RSC Advances

ROYAL SOCIETY OF CHEMISTRY

www.rsc.org/advances

Journal Name

ARTICLE

Controlled synthesis of barium chromate multi-layered microdiscs and their photocatalytic activity

Received 00th January 20xx,
Accepted 00th January 20xx

DOI: 10.1039/x0xx00000x

www.rsc.org/

Mattawan Japa, [a] Patchareeporn Panoy, [a] Supanan Anuchai, [a] Sukon Phanichphant, [b] Piyarat Nimmanpipug, [a] Sulawan Kaowphong, [a] Doldet Tantraviwat[c] and Burapat Inceesungvorn[a,*]

$BaCrO_4$ microdiscs composed of multi-layered microplates were successfully synthesized by a facile oxalate-assisted precipitation method for the first time. Herein, the oxalate ion helps slow down the nucleation rate of $BaCrO_4$ crystals by complexing with barium ion and offers a control over crystal growth and self-assembly processes *via* selective adsorptions probably on the facets containing elevated barium ions of the growing $BaCrO_4$ crystals. Based on the time-dependent experiments, the dissolution–recrystallization–self-assembly process has been proposed for a possible formation mechanism of the multi-layered microdiscs. Preliminary photocatalytic study suggests that the multilayered microdisc preferentially degrade methyl orange over methylene blue and phenol due to its positive surface charge. Further investigation on MO degradation performance under UV and visible irradiations clearly shows that the three-dimensional hierarchical structure provides better photocatalytic activity than its low-dimensional counterpart, potentially due to its higher optical absorption ability originated from the unique morphology. The synthetic method developed in this work not only provides a one-step, facile and effective control over the morphology of $BaCrO_4$, but also offers an alternative approach toward the design of efficient photocatalytic materials.

1. Introduction

Barium chromate ($BaCrO_4$), an analogue of barite crystal ($BaSO_4$), has attracted significant attention because of its promising applications as an excellent oxidizing agent, a catalyst for gas-phase oxidation reactions and a photocatalyst [1, 2]. $BaCrO_4$ has shown an ability to degrade methylene blue dye, eosin yellow and azure B under visible light [3–5]. However, due to its narrow band gap energy of ~2.63 eV [4], the electron–hole recombination rate is also high, hence limiting the photoactivity and hindering its practical application. Therefore, an attention has been paid considerably on the enhancement of its photocatalytic activity [2].

Synthesis of inorganic crystals with controlled size and morphology has been extensively pursued over the past few decades because of the powerful potential in designing materials with tunable physicochemical properties to serve various technological applications [6–9]. By changing the size and shape of materials, their chemical and physical properties can be tailored according to the variation of atomic arrangements in each exposed crystal facets. As a result of their complex morphology and large surface area, three-dimensional (3D) hierarchical structures usually offer more active sites or favorable charge transport pathways, which lead to properties superior to their spherical counterparts [10–12]. Therefore, an exploration for the efficient and well-controlled synthesis of functional materials with complex 3D nano/microstructures is still a hot research topic and remains as a big challenge for materials chemistry researchers.

Several strategies have been used to prepare $BaCrO_4$ hierarchical structures such as Langmuir-Blodgett method [13] and reverse micelle and microemulsion technique [6, 7, 14, 15], however, the template-directing approach [8, 9, 16–20] is viewed as one of the most versatile and efficient ways for the rational design of 3D architectures. Many organic templates, especially both synthetic [6–9] and natural polymers [18, 19], have previously been employed in the morphosynthesis of $BaCrO_4$ and various well-defined morphologies have been found, including rectangular superlattices, nanofilaments and single-crystal fibers [8, 9], X-shaped particles, nanofiber bundles and multi-funnel-like superstructures [8, 17], feather-like superstructures [18], shuttle-shaped particles [20], and 3D dendrites [15, 19]. However, to the best of our knowledge, the use of sodium oxalate as a crystal growth modifier and the formation of hierarchical disc-like microstructures as obtained in this present work have never been reported.

Herein, the $BaCrO_4$ multi-layered microdiscs were successfully prepared by a simple oxalate-assisted precipitation method. The presence of oxalate ion and its concentration were crucial for the formation of such unique assembly. In order to elucidate the crystal growth processes, structural and morphological transformation from barium oxalate precursor to barium chromate product were systematically investigated. Accordingly, a possible formation mechanism for the multi-layered discs was proposed and discussed. In addition, photocatalytic activity of the obtained hierarchical discs was also evaluated in comparison with its bulk counterpart.

2. Experimental

[a] *Department of Chemistry, Faculty of Science, Chiang Mai University, Chiang Mai 50200, Thailand. Email: binceesungvorn@gmail.com*
[b] *Materials Science Research Center, Faculty of Science, Chiang Mai University, Chiang Mai, 50200, Thailand.*
[c] *Department of Electrical Engineering, Faculty of Engineering, Chiang Mai University, Chiang Mai, 50200, Thailand and Thai Microelectronics Center (TMEC), National Electronics and Computer Technology Center (NECTEC), Chachoengsao 24000, Thailand.*

Electronic Supplementary Information (ESI) available: TEM images and SAED patterns of $BaCrO_4$ obtained under different $Ba^{2+}/C_2O_4^{2-}$ molar ratios and Zeta potential of $BaCrO_4$ discs as a function of pH. See DOI: 10.1039/x0xx00000x

2.1 Preparation of $BaCrO_4$ multi-layered microdiscs

All chemicals were of analytical grade reagents and used as received without further purification. In a typical procedure, 2 mmol of barium acetate ($Ba(CH_3COO)_2$) and 4 mmol of sodium oxalate ($Na_2C_2O_4$) were separately dissolved in 10 ml of distilled water. In another beaker, 50 ml of aqueous solution containing 1 mmol of potassium dichromate ($K_2Cr_2O_7$) was prepared and the solution pH was adjusted to 7 using 1.0 M NaOH solution. At this pH, the orange red solution of dichromate ion changed to the bright yellow solution of chromate ion. Upon mixing of the $Ba(CH_3COO)_2$ and $Na_2C_2O_4$ solutions, white precipitates were immediately formed. After stirring the mixture for 30 min, the chromate solution was added dropwise and the yellow precipitates were readily obtained. The solution pH was again adjusted to 7. After aging for 24 h at room temperature, bright yellow precipitates were collected, washed with distilled water several times and dried at 70 °C overnight.

2.2 Characterizations and photocatalytic activity tests

Crystal structure of the samples was studied by X-ray diffraction (XRD) on Rigaku MiniFlex II diffractometer using Cu Kα radiation (1.54 Å). Field emission scanning electron micrographs (FESEM) were recorded on JEOL JSM-6335F. Transmission electron microscopy (TEM) and selected-area electron diffraction (SAED) measurements were carried out on JEOL JEM-2010. Fourier transformed infrared (FTIR) spectroscopy was performed on Bruker TENSOR27 using the KBr pellet technique. Point of zero charge of the obtained sample was examined by Zetasizer Nano ZSP (Malvern Instruments). Photocatalytic activities of the material under UV and visible light were studied by using 20 W UV lamp and Halogen lamp (Phillips) equipped with a 400 nm cut-off filter as light sources. Different organic molecules including methyl orange (MO), methylene blue (MB) and phenol were chosen as model compounds for the preliminary photocatalytic degradation study. In a typical run, 0.1 g of catalyst was dispersed in an aqueous solution of an organic pollutant (1×10^{-5} M, 100 ml). Prior to light irradiation, the catalyst was stirred under the dark for 1 h to obtain adsorption–desorption equilibrium. At a given time interval, 2 ml samples were taken from the reaction solution and the amount of MO and MB were determined by Shimadzu UV-1800 spectrophotometer at 465 nm and 660 nm, respectively. The amount of phenol was also analyzed by measuring absorbance at 510 nm after color development by 4-aminoantipyrine standard method [21, 22].

3. Results and discussion

3.1 Structure and morphology of barium oxalate precursor

At the early stage of the synthesis process, white barium oxalate precipitates are readily formed upon the addition of $Na_2C_2O_4$ into $Ba(CH_3COO)_2$ solution because of its low solubility in water. The composition and phase purity of the barium oxalate precursor are characterized by XRD and FTIR as shown in Fig. 1a and b, respectively. The diffraction pattern can be indexed to triclinic $BaC_2O_4{\cdot}0.5H_2O$ (ICDD 00–020–0134) with lattice constants a = 8.748 Å, b = 9.298 Å and c = 6.170 Å. A trace impurity due to $Ba(CH_3COO)_2$ (ICDD 00–020–0131) can also be observed. FTIR spectrum of the $BaC_2O_4{\cdot}0.5H_2O$ precursor (Fig. 1b) agrees very well with those reported previously [23, 24]. The band at 3448 cm^{-1} and 1636 cm^{-1} can be assigned respectively to stretching and bending vibrations of the hydrated or physically adsorbed water [23–26]. The bands at 1592 cm^{-1} and 1420 cm^{-1} due to $\nu_{as}(COO)^-$ and $\nu_s(COO)^-$ of either oxalate or acetate are also observed [24]. Another two bands at 1328 cm^{-1} and 1313 cm^{-1} can be respectively ascribed to $\nu_s(C{=}O) + \nu_s(C{-}C)$ and $\nu_s(C{-}O) + \delta(O{-}C{=}O)$ of the chelating oxalate group [24, 26]. The characteristic sharp absorption band of $BaC_2O_4{\cdot}0.5H_2O$ due to $\nu(Ba{-}O) + \delta(O{-}C{=}O)$ can be clearly seen at 775 cm^{-1} [24, 26]. FESEM images of the $BaC_2O_4{\cdot}0.5H_2O$ precursor (Fig. 2a and b) present sheaflike assemblies with a length of about 25 μm. A high magnification image (Fig. 2b) shows that the sheaf structure is actually composed of many thin microrods that aggregate side-by-side with each other along their long-axis direction, and branch off at both ends of the assemblies. The presence of short and uncombined rods, indicated by red arrows in Fig. 2a and b, also supports that the microrods act as building blocks of the sheaflike $BaC_2O_4{\cdot}0.5H_2O$ assemblies. Unfortunately, TEM image of the barium oxalate precursor could not be obtained because the sample quickly decomposes under an electron beam irradiation.

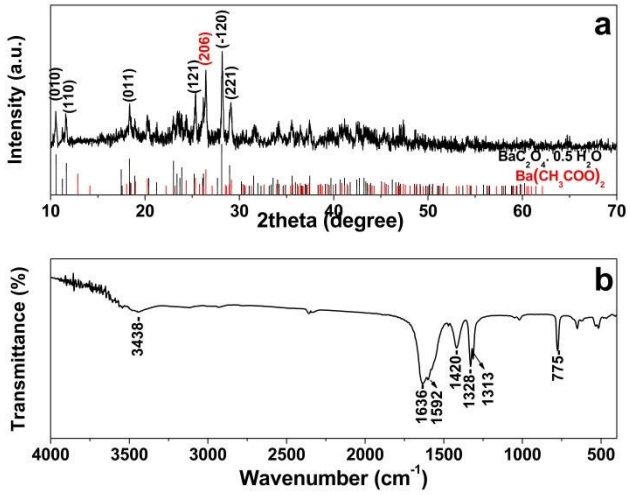

Fig. 1 (a) XRD pattern and (b) FTIR of barium oxalate hemihydrate precursor.

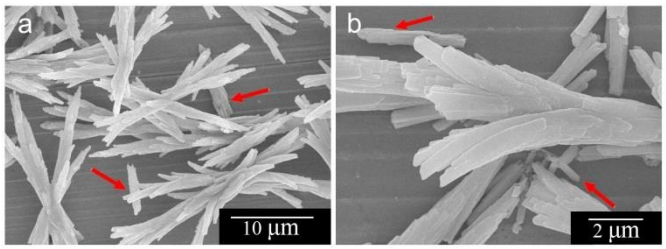

Fig. 2 (a) Low and (b) high magnification FESEM images of barium oxalate hemihydrate precursor.

3.2 Structure and morphology of barium chromate product

Upon the addition of chromate ion containing solution into the $BaC_2O_4{\cdot}0.5H_2O$ precursor suspension, the yellow precipitates of barium chromate are immediately formed. Fig. 3a and b respectively present XRD pattern and IR spectrum of the product after aging at room temperature for 24 h. The diffraction pattern can be indexed to orthorhombic $BaCrO_4$ (ICDD 01–078–1401) with lattice constants a = 9.113 Å, b = 5.528 Å and c = 7.336 Å. No peaks of barium oxalate precursor and other impurities are observed, indicating the high phase purity of the as-obtained $BaCrO_4$ products. The XRD results clearly suggest that the phase

transformation from $BaC_2O_4{\cdot}0.5H_2O$ precursor to $BaCrO_4$ phase is successfully achieved under the reaction conditions applied. FTIR spectrum of the sample (Fig. 3b) demonstrates the characteristic absorption bands at 920 and 860 cm^{-1} due to Cr–O stretching vibrations of CrO_4^{2-} [19]. The band due to Ba–O stretching in $BaCrO_4$ is also found at 422 cm^{-1} [27]. Additionally, no characteristic band of the $BaC_2O_4{\cdot}0.5H_2O$ precursor at 775 cm^{-1} is found, supporting the complete phase transformation from the oxalate precursor to the chromate product as evidenced previously from the XRD study. Since the negatively charged ions of the group –COOH can adsorb on specific planes of $BaCrO_4$ [8], the three additional bands observed at *ca.* 1584, 1400 and 1321 cm^{-1} are likely ascribed to the different vibrations of oxalate anions, which are physically adsorbed on the $BaCrO_4$ surfaces. This implies that the oxalate ion may play a crucial role in the formation of $BaCrO_4$ hierarchical structure *via* a selective adsorption on the $BaCrO_4$ crystal surfaces.

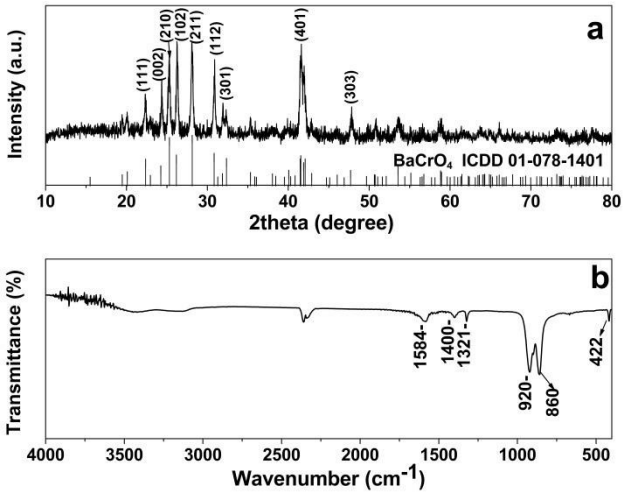

Fig. 3 (a) XRD pattern and (b) FTIR of barium chromate product at 24 h.

A panoramic FESEM image of the $BaCrO_4$ product (Fig. 4a) demonstrates a large quantity of uniform multi-layered disc structures with diameters of 7–8 μm. Close observation on the surface (Fig. 4b) and a side view image (Fig. 4c) of an individual microdisc reveal that the disc is built from many semicircular plates with an average thickness of 50 nm, which are densely packed to form a multi-layered structure. As seen from the top view image in Fig. 4b, the 2D plates seem to fuse together at the center of the microdisc, producing a rather smooth platform in the middle section. Further characterization of the hierarchical disc architectures is carried out by TEM and SAED investigations. The TEM image of an individual disc in Fig. 4d indicates that the disc has a diameter of about 7 μm, being consistent with that observed from the SEM study. Different contrast between the central and the fringe parts of the disc confirms that the microplates are inter-connected tightly and densely packed at the center. Its corresponding SAED pattern (Fig. 4e) shows an arc-like spot pattern, implying that the polycrystalline microdisc is constructed by many single-crystalline building units. The HRTEM image (an inset of Fig. 4e) taken from the edge of the plate (area 1) in Fig. 4d exhibits an interplanar spacing of about 0.46 nm which corresponds to the (200) crystal face of $BaCrO_4$, thus confirming the single-crystal nature of the plate building unit. Another SAED pattern (Fig. 4f) taken from area 2 in Fig. 4d also demonstrates a single crystalline characteristic with a view along $[1\bar{2}0]$ zone axis. This further

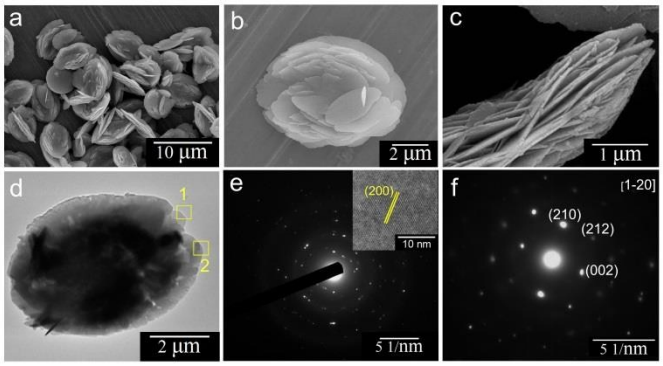

Fig. 4 (a–c) FESEM images of barium chromate product, (d) TEM micrograph and (e) the corresponding SAED pattern of an individual microdisc, the inset in (e) is the HRTEM image of a single plate building unit taken from area 1 in (d). (f) SAED pattern of the edge area of the disc taken from area 2 in (d).

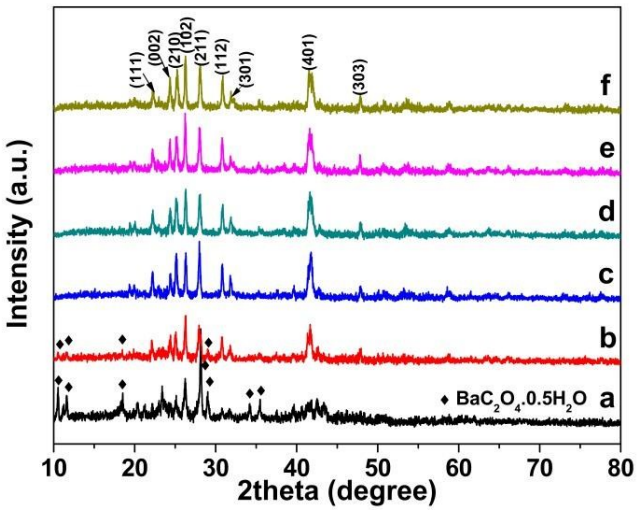

Fig. 5 XRD patterns of the samples collected at different reaction times: (a) 5 min, (b) 15 min, (c) 30 min, (d) 1 h, (e) 6 h and (f) 12 h.

suggests that the exposed surface of the plate is $(1\bar{2}0)$ face. It has previously been reported that the $(1\bar{2}0)$ facet of $BaCrO_4$ contains slightly elevated barium ions and the negatively charged group of –COOH is favorably adsorbed on this face and blocks it from further growth [8, 9]. Therefore, it is possible that the oxalate ion present in this work may adsorb on the $(1\bar{2}0)$ face *via* electrostatic attraction, thus inhibiting the growth of this plane and leaving the $(1\bar{2}0)$ facet as an exposed face of the 2D plate.

3.3 Time-dependent XRD and SEM studies

To reveal the growth process of $BaCrO_4$ hierarchical microdiscs, time-dependent experiments were carefully performed. The intermediate samples were collected at different reaction times, and their crystal structure and morphology were subjected to XRD and FESEM investigations. The structural evolution obtained from XRD study at different growth stages are presented in Fig. 5. As seen from the figure, the intermediate sample at 5 min after the addition of chromate ion (Fig. 5a) contains a majority of $BaC_2O_4{\cdot}0.5H_2O$ precursor and a minority of $BaCrO_4$ product. As the reaction time is increased to 15 min (Fig. 5b), the diffraction peaks due to $BaC_2O_4{\cdot}0.5H_2O$ phase are significantly decreased, leaving the $BaCrO_4$ phase as a main component. After 30 min of the reaction

(Fig. 5c), only $BaCrO_4$ phase can be found, suggesting that a complete transformation of $BaC_2O_4{\cdot}0.5H_2O$ precursor to $BaCrO_4$ product may be attained at this stage. This observation also implies that the dissolution of $BaC_2O_4{\cdot}0.5H_2O$ and the recrystallization of $BaCrO_4$ in the system being studied are rather fast because the phase transformation can be accomplished within 30 min. Further prolonging the reaction time to 1, 6 and 12 h (Fig. 5d–f) only leads to a variation of the relative peak intensity, which suggests that the $BaCrO_4$ at different growth stages may have various preferred orientations, hence different sizes and shapes could be observed.

Morphological evolution of the samples at different stages is presented in Fig. 6. At the beginning, the sheaflike assemblies of $BaC_2O_4{\cdot}0.5H_2O$ microrods are formed as shown previously in Fig. 2. The sample at 5 min after the addition of chromate ion develops 2D circular microplates on the sheaf precursor (Fig. 6a). The plate thickness and diameter are about 30–40 nm and 2–3 μm, respectively. The $BaC_2O_4{\cdot}0.5H_2O$ microrod building units are also smaller in size compared with those before chromate addition. Upon considering the time-dependent XRD results in Fig. 5a where the $BaCrO_4$ product emerges at this stage, it is likely that the circular plates belong to the $BaCrO_4$ phase. As increasing the reaction time to 15 min (Fig. 6b), a minority of rod $BaC_2O_4{\cdot}0.5H_2O$ precursor, marked by yellow circle, can be seen together with a large amount of intercrossed $BaCrO_4$ microplates. This observation agrees well with the XRD results in Fig. 5b where a trace amount of $BaC_2O_4{\cdot}0.5H_2O$ precursor is found together with a majority of $BaCrO_4$ phase. Additionally, some large plates also have several small semicircular platelets grown from their flat surfaces. The plate diameter (*ca.* 3.5 μm) is slightly larger than that at the shorter reaction time. As the reaction proceeds for 30 min (Fig. 6c), the sample shows the coexistence of small flower-like microspheres and undeveloped disc-like architectures. The flowery microstructures with diameters of about 1–2 μm are constructed from many intercrossed plates with thicknesses of 40–60 nm. The microdiscs attained at this stage (an average diameter of *ca.* 3–4 μm) are still underdeveloped as some discs consist of only a few lamellas. The magnified SEM image (an inset of Fig. 6c) also supports that the disc-like structures at this reaction time are at their intermediate stage as the lamellas cannot develop clear edges and only a few layers can be seen. The rodlike precursor cannot be found at this stage, which corresponds well to the disappearance of the $BaC_2O_4{\cdot}0.5H_2O$ phase in the XRD pattern (Fig. 5c).

When the reaction time is increased to 1 h (Fig. 6d), larger microflowers and microdiscs with average diameters of 4 and 5 μm, respectively, are presented. The thicknesses of the 2D plate assembling units of both structures are also increased to 90–100 nm. Upon prolonging the reaction time to 6 h (Fig. 6e), a minority of crossed microplatelets is found instead of the flower-like structures. At the same time, the microdiscs grow gradually in size and also develop clear lamella structures as seen from the inset of Fig. 6e. As the reaction proceeds to 12 h (Fig. 6f), the multi-layered discs become a predominant product. The size of the discs also increases to 6–7 μm. At this stage, the crossed microplates are rarely seen. Further increasing the reaction time to 24 h eventually leads to a fully-grown multi-layered microdisc with an average diameter of 7–8 μm as shown previously in Fig. 4a. The sample at this stage is composed entirely of the multi-layered disc-like structure. No microflower or intercrossed microplatelet is observed at this reaction time.

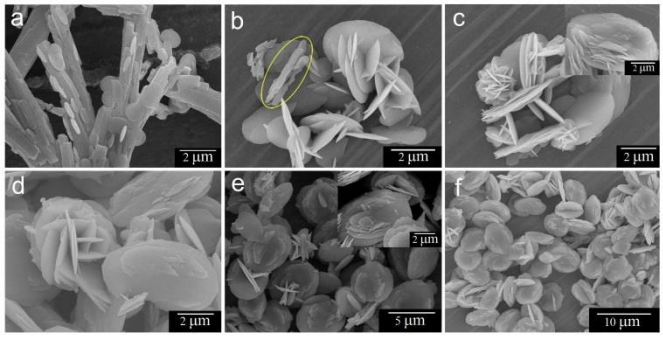

Fig. 6 FESEM images of the samples collected at different reaction times: (a) 5 min, (b) 15 min, (c) 30 min, (d) 1 h, (e) 6 h and (f) 12 h.

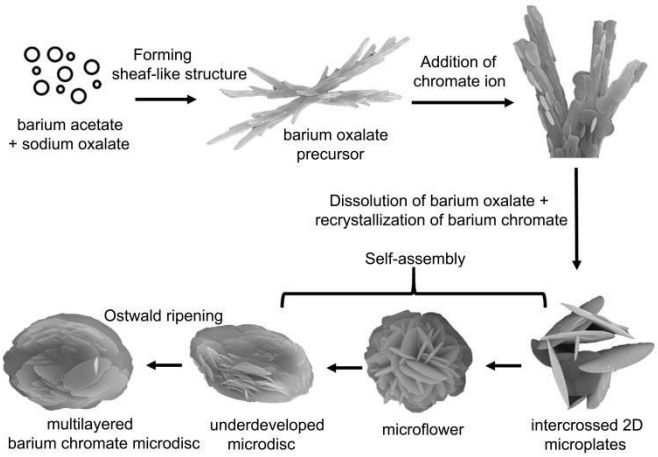

Fig. 7 Schematic illustration for the possible formation mechanism of hierarchical $BaCrO_4$ microdiscs.

3.4 Growth mechanism

On the basis of the time-dependent XRD and SEM results, we propose a dissolution–recrystallization–self-assembly growth mechanism for the formation of $BaCrO_4$ multi-layered microdiscs from the sheaflike $BaC_2O_4{\cdot}0.5H_2O$ precursor as shown in Fig. 7. A similar growth process was also found in the formations of nest-like $BaMoO_4$ crystals [28] and *t*-selenium nanotubes [29].

As already known, the oxalate ion ($C_2O_4^{2-}$) has been widely used as a complexing agent in the preparation of many metal oxides because of the excellent chelating ability of the two carboxyl groups that act as binding sites [26, 30–32]. Therefore, the generation of $BaC_2O_4{\cdot}0.5H_2O$ precipitates at the beginning of the process is likely due to the strong chelating ability of oxalate with Ba^{2+} ion in a supersaturated solution. Once the tiny $BaC_2O_4{\cdot}0.5H_2O$ nuclei are formed, the crystal growth is followed. The growth of $BaC_2O_4{\cdot}0.5H_2O$ microrod building unit was previously ascribed to its intrinsic triclinic structure and the selective adsorption of ions, probably acetate, on specific crystal facets, thus leading to the anisotropic growth [33]. As a result of a continuous self-assembly which is driven by the minimization of the interfacial surface energy [34], the obtained $BaC_2O_4{\cdot}0.5H_2O$ microrods are connected with each other to finally form the sheaflike microstructure.

After the addition of CrO_4^{2-}, both structural and morphological transformations from the $BaC_2O_4{\cdot}0.5H_2O$ to the $BaCrO_4$ microdisc product can be clearly observed as shown previously in Fig. 5 and 6. Since the formation of $BaC_2O_4{\cdot}0.5H_2O$ precipitate could greatly decrease the free Ba^{2+} ion concentration in the solution, therefore the main formation mechanism of $BaCrO_4$ is likely related to the

dissolution of $BaC_2O_4{\cdot}0.5H_2O$ and the recrystallization of $BaCrO_4$. The driving force for this phase transformation is probably due to a much lower solubility product constant of $BaCrO_4$ ($K_{sp} = 1.6\times10^{-10}$) compared with that of $BaC_2O_4{\cdot}0.5H_2O$ ($K_{sp} = 2.18\times10^{-7}$) [35]. At the early stage, the dissolution of $BaC_2O_4{\cdot}0.5H_2O$ gradually releases Ba^{2+} and $C_2O_4^{2-}$ ions back into the solution (Eq. 1). This helps control the free Ba^{2+} ion concentration and slow down the nucleation rate of $BaCrO_4$ nanocrystals (Eq. 2) which could facilitate the subsequent growth of 3D hierarchical architectures in view of the kinetic process [36].

$$BaC_2O_4{\cdot}0.5H_2O \rightarrow Ba^{2+} + C_2O_4^{2-} + 0.5H_2O \quad (1)$$
$$Ba^{2+} + CrO_4^{2-} \rightarrow BaCrO_4\downarrow \quad (2)$$

The nucleation of $BaCrO_4$ would readily start from the regions with a relatively high Ba^{2+} concentration, which is likely on the surface of the $BaC_2O_4{\cdot}0.5H_2O$ precursor where the dissolution process occurs. This assumption is supported by the presence of many thin circular $BaCrO_4$ plates on the sheaflike structure rather than the formation of individual $BaCrO_4$ plates as evidenced from the SEM image in Fig. 6a. The newly formed $BaCrO_4$ nuclei are not stable due to their high chemical potentials, so they prefer to grow into larger particles [37]. The larger particles grow at the expense of the smaller ones because of the different solubilities between the larger and the smaller particles according to the Gibb-Thomson law [34, 38]. During this growth stage, the free oxalate anions could selectively bind to the faces with elevated barium ions of the growing crystals. This would disturb the intrinsic growth habit of the $BaCrO_4$ crystal, leading to the growth along some preferred directions and the formation of the plate-like morphology as a consequence.

Upon prolonging the reaction time, the dissolution of $BaC_2O_4{\cdot}0.5H_2O$ further proceeds, thus releasing more Ba^{2+} ions to react with the vicinal CrO_4^{2-} ions. Therefore, the disappearance of $BaC_2O_4{\cdot}0.5H_2O$ rod assemblies and the formation of larger $BaCrO_4$ plates can be observed. In the further growth stage, the fact that oxalate ion is an efficient structure-directing agent plays an important part in directing the growth and self-assembly of the microplates into microflowers and finally microdiscs, which are probably driven by the minimization of surface free energy [15, 28, 30, 39]. As a result of Ostwald ripening process, the size of the disc increases gradually and the morphology further develops clear edges and multi-layered architectures. Eventually, no microflower remains and the product is composed entirely of 3D multi-layered disc structure when the reaction lasts more than 12 h.

Our experimental results also show that the amount of $C_2O_4^{2-}$ ion plays a crucial role in determining the crystal growth habit, the particle assembly, and the final product morphology as presented in Fig. 8. In the absence of oxalate ions (Fig. 8a), irregularly shaped microplates with the thickness of ~0.2 μm are observed. However, in the presence of oxalate ions, the architecture of $BaCrO_4$ varies remarkably with the amount of oxalate. When the molar ratio of $Ba^{2+}/C_2O_4^{2-}$ is equal to 1: 0.5 (Fig. 8b), the product appears as random aggregates of nonuniform microplates with the plate thicknesses of ~0.6 μm. As increasing the $Ba^{2+}/C_2O_4^{2-}$ to 1: 1 (Fig. 8c), the bundle-like assemblies of nearly circular plates are clearly observed. A close-up observation (an inset of Fig. 8c) reveals that the bundle is actually built from numerous orderly packed microplates with the thicknesses of ~0.2 μm and the microplates are packed together through side-by-side and plane-to-plane conjunctions to create the length and width dimensions of the bundle-like structure, respectively.

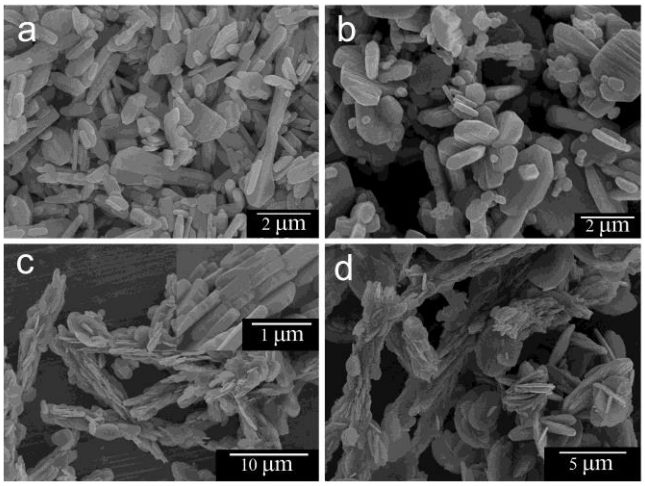

Fig. 8 FESEM images of the products obtained in the presence of different $Ba^{2+}/C_2O_4^{2-}$ molar ratios: (a) 1: 0, (b) 1: 0.5, (c) 1: 1 and (d) 1: 1.5.

Upon increasing the $Ba^{2+}/C_2O_4^{2-}$ to 1: 1.5 (Fig. 8d), the products take on three different morphologies; a bundle-like assembly as observed previously, a random aggregate of microplates and an undeveloped disc-like structure. Note that the thickness of the microplates obtained under different synthesis conditions cannot be compared because the crystal growth behavior and growth rate of each facets under those conditions are varied due to differences in the relative order of surface energies [40, 41]. Additionally, TEM and SAED results (Fig. S1) clearly show that the exposed surfaces of $BaCrO_4$ microplates under the absence and presence of oxalate ions are different. When the $Ba^{2+}/C_2O_4^{2-}$ molar ratio is equal to 1: 0 (Fig. S1 a, b), the exposed facet is $(\bar{2}10)$ plane which is a neutral surface [8]. However, when the $Ba^{2+}/C_2O_4^{2-}$ molar ratios are equal to 1: 0.5 (Fig. S1 c, d) and 1: 1 (Fig. S1 e, f), the exposed planes are $(\bar{1}20)$ and $(1\bar{2}0)$, respectively, which are positive faces [8]. Since the plates under those conditions have different exposed facets and that the thicknesses of those plates lie in different crystallographic directions where various crystal growth rates could be attained, therefore a comparison based on thickness of the samples synthesized under different conditions would lead to misunderstanding. The XRD results in Fig. 9 indicate that pure $BaCrO_4$ products, but with different crystallinity and preferred orientations, are also obtained upon varying the oxalate amounts.

It is possible that, when the solution contains low oxalate concentration, the complexing action of $C_2O_4^{2-}$ with Ba^{2+} ion is not completed, thus leaving high concentration of Ba^{2+} ions available in the solution. Therefore, the fast nucleation and crystal growth rates of $BaCrO_4$ could be attained. This also restricts the structure-directing ability of the $C_2O_4^{2-}$ which leads to nonuniform and ill-defined structures. However, when the oxalate ion concentration is high enough as in the case of $Ba^{2+}/C_2O_4^{2-}$ equal to 1: 2, the extremely low concentration of free Ba^{2+} ions and the slow release of Ba^{2+} ions from the $BaC_2O_4{\cdot}0.5H_2O$ dissolution step are advantageous for the growth of 3D hierarchical structures. In this case, the excessive adsorption of oxalate on the surfaces of $BaCrO_4$ crystals helps reduce the aggregation potential and the assembly styles, which are necessary for the formation of uniform and well-defined hierarchical architectures [34].

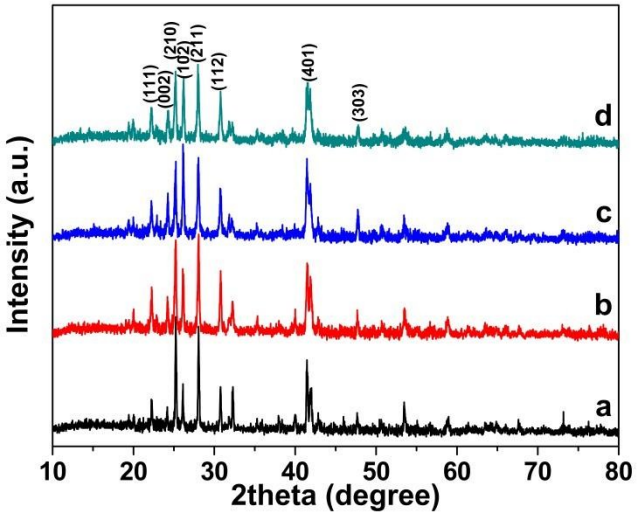

Fig. 9 XRD patterns of products obtained in the presence of different $Ba^{2+}/C_2O_4^{2-}$ molar ratios: (a) 1: 0, (b) 1: 0.5, (c) 1: 1 and (d) 1: 1.5.

According to the above results, the oxalate ion plays two important roles in the morphology-controlled synthesis of the $BaCrO_4$ multi-layered microdisc. First, it serves as a strong coordinating agent with Ba^{2+} ion, which further kinetically controls the nucleation and growth rates of $BaCrO_4$ crystals during the dissolution–recrystallization step. Second, it acts as a structure-directing agent *via* a selective adsorption on specific $BaCrO_4$ facets, probably those containing elevated barium ions. As a result, the growth behavior and self-assembly mechanism are altered and thus lead to the unique morphology as observed in this study. It should also be noted that the mechanism proposed in this work is just a tentative explanation for the experimental results. The exact formation mechanism of the hierarchical $BaCrO_4$ microdiscs still needs further investigation because several factors such as solution pH, the amount of barium and chromate ions, crystal-face attractions, van der Waals forces, electrostatic interactions and hydrogen bonds may affect the growth and self-assembly processes as well [12, 30, 34].

3.5 Optical property and pore distribution

Fig. 10 displays UV–vis diffuse reflectance spectra of $BaCrO_4$ multi-layered discs in comparison with the commercial TiO_2 P25 and the irregular $BaCrO_4$ microplates synthesized without the oxalate addition. Although both microdiscs and microplates show weaker UV absorption than the TiO_2, their visible-light-harvesting ability may provide the materials with better photoactivity under visible light. The absorption onsets of microdiscs and microplates are 484 nm and 495 nm, which correspond respectively to the band gap energies of 2.56 eV and 2.50 eV, according to the equation $E_g = 1240/\lambda_{edge}$, where E_g is the band gap energy of the semiconductor and λ_{edge} is the light absorption edge of the semiconductor [42]. In spite of its slightly wider band gap energy, the discs show obviously stronger UV and visible light absorptions than the plates, which would be beneficial for an enhanced photocatalytic performance of the material. The observed band gap energies are slightly different from that reported in Ref. 4 (2.63 eV), possibly due to differences in size and shape of the $BaCrO_4$. As seen from Fig. 11, the isotherms of both microdiscs and microplates can be regarded as type IV, indicating the presence of mesopores (2–50 nm in size) according to

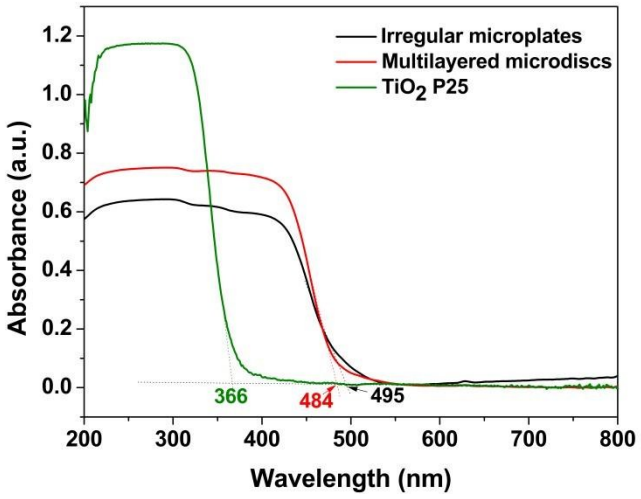

Fig. 10 UV–vis diffuse reflectance spectra.

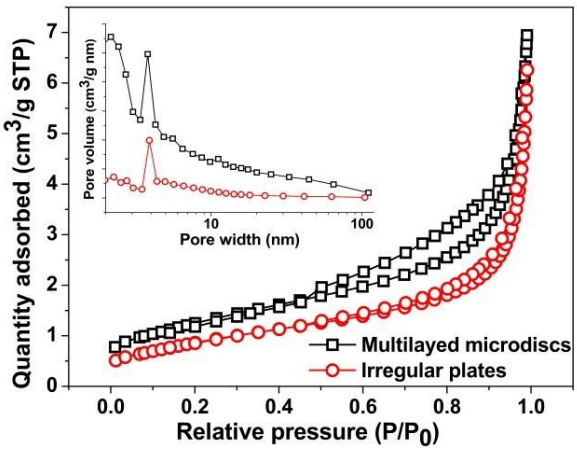

Fig. 11 N_2 adsorption–desorption isotherms and pore size distribution curves.

the IUPAC classification. BET surface areas of the discs and plates are 4.42 and 3.07 $m^2 g^{-1}$, respectively. The type H_3 hysteresis loop as clearly seen from the multi-layered disc structures also indicates the presence of slit-shaped pores originated from the aggregation of plate-like particles [43]. The pore size distribution curves (an inset of Fig. 11) derived from Barrett–Joyner–Halenda (BJH) calculation of desorption branches also confirm the mesoporous structure of both microdiscs and microplates.

3.6 Photocatalytic performances

Photocatalytic activity of the hierarchical microdiscs was also studied *via* MO, MB and phenol degradations under UV and visible light as shown in Fig. 12a and b, respectively. The MO, MB and phenol degradation activities under UV light are 36%, 24%, and 12%, respectively, whereas those under visible light are 29%, 17% and 9%, respectively. The photocatalytic performance under UV light is higher than that under visible light in all cases. This is probably because the main light absorption range of the $BaCrO_4$ is in the UV region, therefore irradiation in this range could effectively activate the catalyst, and hence a better activity than that under visible light could be attained. The results also indicate that the discs preferentially degrade MO rather than MB and phenol. This could be explained based on an investigation on the surface charge of the $BaCrO_4$ discs as presented in Fig. S2.

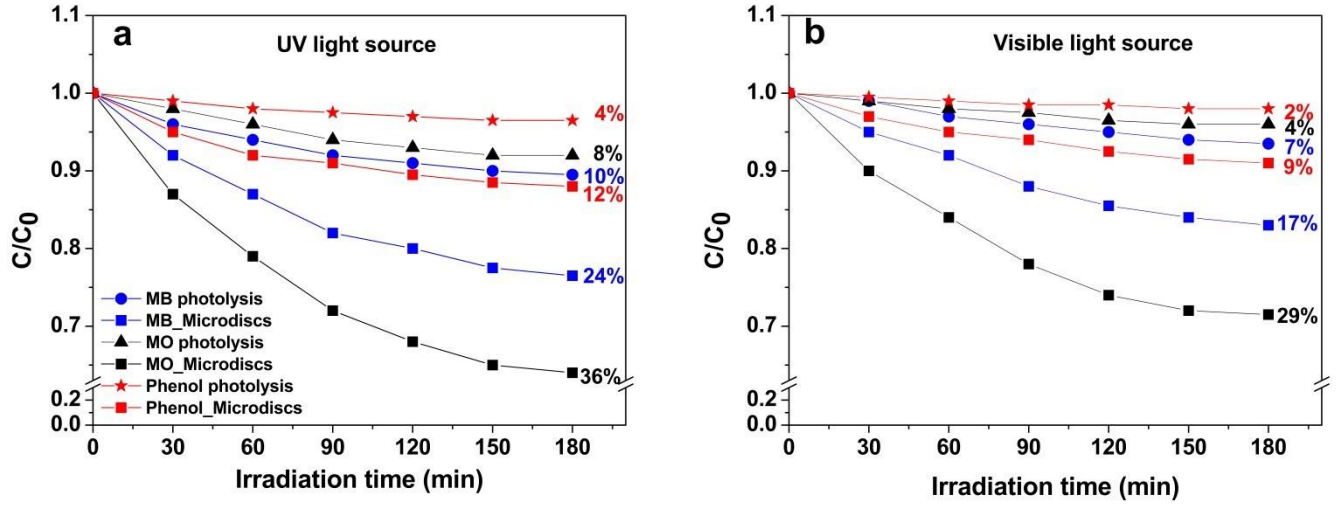

Fig. 12 photocatalytic degradation of methylene blue (MB), methyl orange (MO) and phenol using $BaCrO_4$ microdiscs under a) UV and b) visible light irradiations.

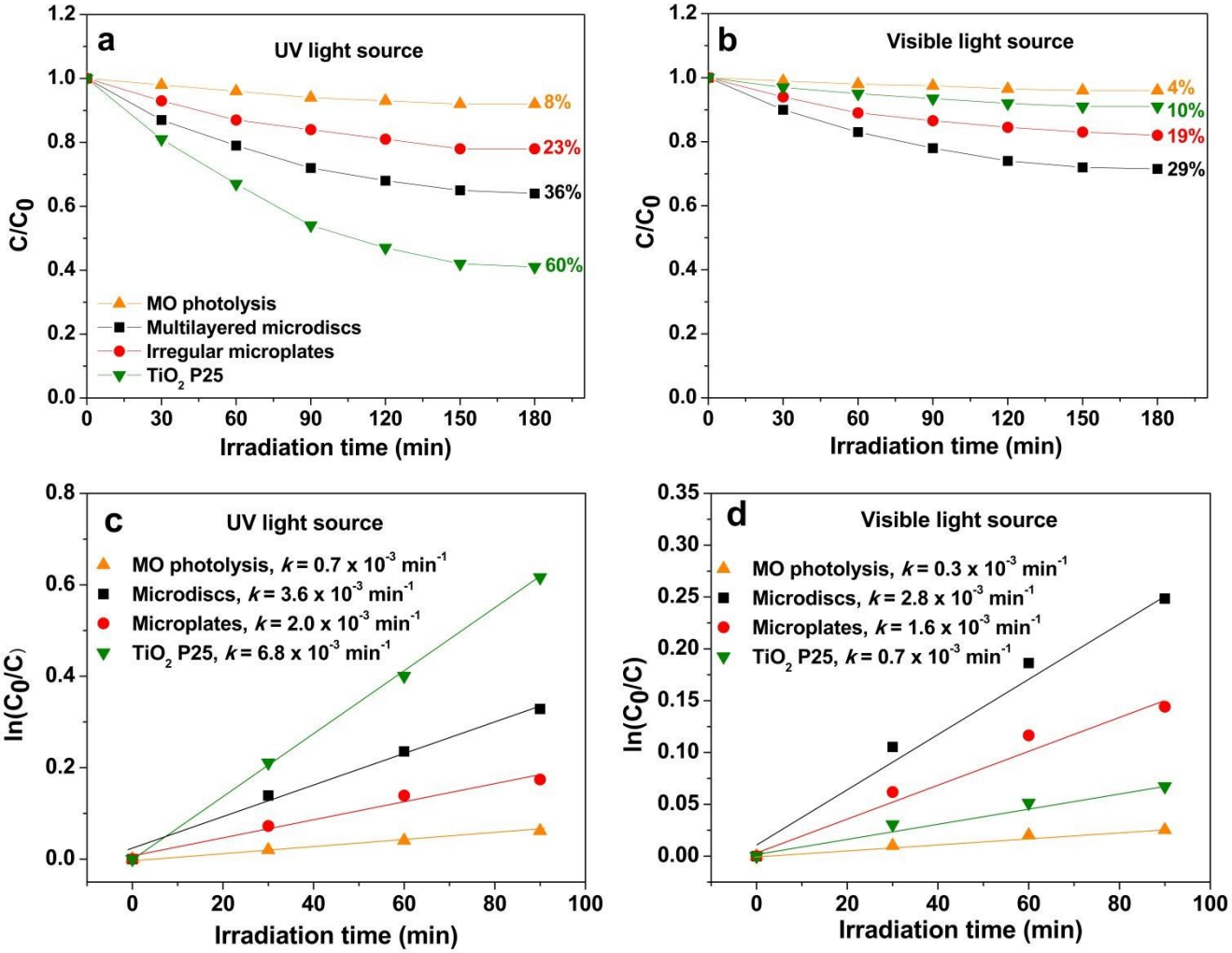

Fig. 13 Photocatalytic degradation and pseudo-first order kinetics of MO under (a, c) UV and (b, d) visible light irradiations.

The result in Fig. S2 indicates that the zeta potential varies from +37.74 mV to -12.87 mV with a point of zero charge at pH of 7.7. Therefore, under the photocatalytic experiment where the solution pH is ~6.5, the $BaCrO_4$ with positive surface charge would preferentially adsorb and degrade anionic methyl orange dye rather than the cationic methylene blue and the neutral phenol molecules. Since the best activity is obtained in the case of MO degradation, therefore the MO dye was chosen for further photocatalytic study.

MO degradation activities of the hierarchical microdiscs under UV and visible light are presented in Fig. 13a and b, respectively. As a comparison, MO photolysis and the photocatalytic activities of the commercial TiO_2 P25 and the $BaCrO_4$ irregular plates obtained in the absence of oxalate ion were also evaluated. The figures show only a slight decrease in MO concentration when MO is exposed to UV and visible light, suggesting that the direct photolysis of MO can be neglected. Under UV irradiation (Fig. 13a), TiO_2 P25 with higher surface area (~50 m^2/g, AEROXIDE) and stronger UV absorption ability provides better MO degradation efficiency than the microdiscs and microplates, respectively. However, under visible light illumination (λ>400) as presented in Fig. 13b, the highest MO degradation activity is found from the microdiscs, following by the irregular plates and the commercial TiO_2 P25, respectively. The photodegradation activity is further studied by using the pseudo-first order kinetic model as follows:

$$\ln\left(\frac{C_0}{C_t}\right) = kt \qquad (3)$$

where C_0 and C_t are the MO concentration at time 0 and t respectively, and k is the apparent pseudo-first order rate constant which is derived from the slope of the linear plot of $\ln(C_0/C)$ versus time (Fig. 13c and d). From Fig. 13c and d, all catalysts under UV light show higher k constants than those under visible light because their main light absorption ranges are in the UV region. It can also be seen that the rate constants for the multilayered discs under both UV and visible are significantly higher than those of the irregular plates, indicating the superior photocatalytic activity of the hierarchical disc over its bulk counterpart. Although the microdiscs have lower crystallinity than the irregular plates as seen from the XRD results in Fig. 9, the slightly higher surface area and especially the stronger optical absorption help improve their photocatalytic activity significantly. Additionally, the assembly of many microplates in the multi-layered disc could offers a large number of pores, and thus providing effective charge and mass transports for the photocatalytic reaction to occur more easily [44]. Multiple reflections of the incoming light within the hierarchical structure also increase the probability of the interactions between photons and photocatalysts, therefore an improved light-harvesting ability of the catalyst could be achieved from this architecture [12, 34]. Recycling tests under UV and visible light are also performed in order to evaluate photocatalytic stability of the multilayered microdiscs. As seen from Fig. 14a and b, only a slight decrease of ~6% and ~5% under UV and visible, respectively, are observed after five catalytic runs. In addition, XRD patterns (Fig. 15) of the recycled microdiscs are very similar to that of fresh catalyst which indicates a relatively high photostability of the discs under both UV and visible illuminations. The photocatalytic results obtained in this present work clearly show that the $BaCrO_4$ hierarchical microdisc exhibits better photocatalytic performance than its bulk counterpart. However, the photocatalytic mechanism and electron–hole transport process of this architecture still need further investigation.

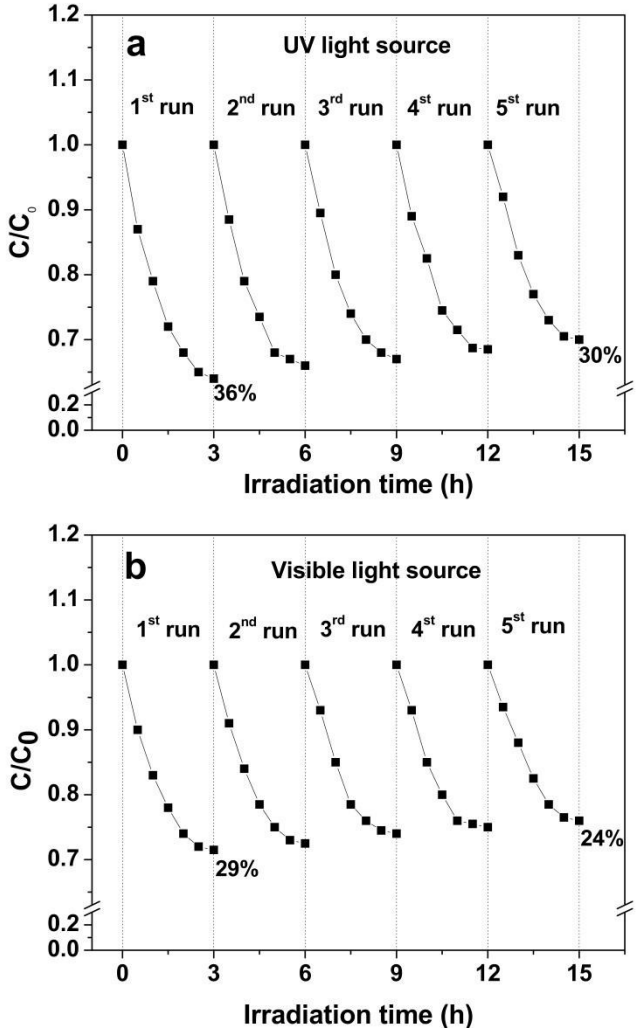

Fig. 14 Stability study of $BaCrO_4$ microdiscs under a) UV and b) visible light.

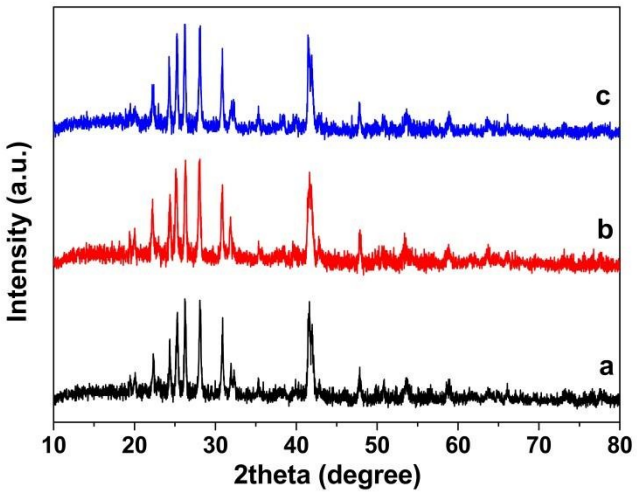

Fig. 15 XRD patterns of $BaCrO_4$ microdiscs a) before and after five recycling runs under b) UV and c) visible light.

4. Conclusions

In summary, multi-layered $BaCrO_4$ microdiscs have successfully been synthesized by a simple oxalate-assisted precipitation method. The complexing and structure-directing abilities of the oxalate ion obviously play crucial roles in the formation of this architecture. Based on the time-dependent experiments, a plausible formation mechanism involving dissolution–recrystallization and self-assembly processes has been proposed. The material is found to favorably degrade MO rather than MB and phenol possibly due to its positive surface charge. A relatively high photostability under UV and visible irradiations is also observed from the multilayered microdiscs. Additionally, the photocatalytic results clearly show that the hierarchical structure can significantly enhance the photoactivity of the material by providing an increased light-harvesting ability and probably efficient transport paths for the reaction to occur. Because of the simplicity and efficient control over the morphology, the present synthetic method may offer an alternative approach toward the morphology-controlled synthesis of other related inorganic materials with uniform 3D hierarchical architecture.

Acknowledgements

This research was financially supported by the Thailand Research Fund (TRF) Grant (TRG5880056), the National Research University Project under Thailand's Office of the Higher Education Commission and the CMU Junior Research Fellowship Program.

References

1. J. Economy, D. T. Meloon, R. L. Ostrozynski. *J. Catal*., 1965, **4**, 446.
2. S. B. Gawande and S. R. Thakare, *Int. Nano Lett*., 2013, **3**, 37.
3. B. Pare, V. Singh and S. B. Jonnalagadda, *Indian J. Chem Sect. A*, 2011, **50**, 1061.
4. S. R. Thakare, S. R. Patil, M. D. Choudhary, *Indian J. Chem. Sect*. A., 2010, **49**, 54.
5. S. Gupta, Diptisoni, Rakshitameta and S. Benjamin, *Chem. Sci. Trans.,* 2015, **4**, 851.
6. M. Li, H. Schnableggar and S. Mann, *Nature*, 1999, **402**, 393.
7. H. Shi, L. Qi, J. ma, H. Cheng and B. Zhu, *Adv. Mater*., 2003, 15, 1647.
8. S.-H. Yu, H. Cölfen and M. Antonietti, *Chem. Eur. J.,* 2002, **8**, 2937.
9. S.-H. Yu, H. Cölfen and M. Antonietti, *Adv. Mater*., 2003, **15**, 133.
10. J. Cui, J. Sun, X. Liu, J. Li, X. Ma and T. Chen, *Appl. Surf. Sci*., 2014, **308**, 17.
11. J. J. Wei, Z. J. Yand and Y. Z. Yang, *CrystEngComm*, 2011, **13**, 2418.
12. J. Chen, D. Li, J. Hu, W. Chen, J. Wang, Y. Hu, X. Fu and Y. Shao, *CrystEngComm*, 2012, **14**, 8382.
13. F. Kim, S. Kwan, J. Akana and P. Yang, *J. Am. Chem. Soc*., 2001, **123**, 4360.
14. Z. Li, J. Zhang, J. Du, B. Han, T. Mu, Y. Gao and Z. Liu, *Mater. Chem. Phys*., 2005, **91**, 40.
15. Y.-S. Cho and Y.-D. Huh, *Mater. Lett.*, 2011, **65**, 3618.
16. W. Chang, Y. Shen, A. Xie and X. Liu, *Appl. Surf. Sci*., 2010, **256**, 4292.
17. Z. Li, J. Zhang, J. Du, B. Han, T. Mu, Y. Gao and Z. Liu, *Mater. Chem. Phys*., 2005, **91**, 40.
18. Y.-S. Cho and Y.-D. Huh, *Mater. Lett.*, 2011, **65**, 3618.
19. W. Chang, Y. Shen, A. Xie and X. Liu, *Appl. Surf. Sci*., 2010, **256**, 4292.
20. S.-H. Yu, M. Antonietti, H. Cölfen and J. Hartmann, *Nano Lett.*, 2003, **3**, 379.
21. American Public Health Association/American Water Works Association/Water Environment Federation, *Standard methods for the examination of water and wastewater*, 14th ed., Washington, DC, USA, 1975.
22. A. Shet and V Shetty K, Environ. Sci. Pollu. Res.(2015), **DOI** 10.1007/s11356-015-5579-z.
23. Y. B. Khollam, S. V Bhoraskar, S. B. Deshpande, H. S. Potdar, N. R. Pavaskar, S. R. Sainkar and S. K. Date, *Mater. Lett*., 2003, **57**, 1871.
24. K. Nakamoto, *Infrared and Raman Spectra of Inorganic and Coordination Compounds*, 5th ed., John Wiley, New York, 1997.
25. N. Deb, *J. Anal. Appl. Pyrolysis*, 2007, **80**, 389.
26. F. Behnoudnia and H. Dehghani, *Dalton Trans.,* 2014, **43**, 3471.
27. L. Andrews and X. Wang, *Inorg. Chem*., 2005, **44**, 11.
28. Z. Luo, H. Li, H. Shu, K. Wang, J. Xia and Y. Yan, *Cryst. Growth Des*., 2008, **8**, 2275.
29. G. Xi, K. Xiong, Q. Zhao, R. Zhang, H. Zhang, and Y. Qian, *Cryst. Growth Des*., 2006, **6**, 577.
30. L. Li, J. Zhao, Y. Wang, Y. Li, D. Ma, Y. Zhao and S. Hou, *J. Solid State Chem*., 2011, **184**, 1661.
31. W. Liu, L. Feng, C. Zhang, H. yang, J. Guo, X. Liu, X. Zhang and Y. Yang, *J. Mater. Chem. A*, 2013, **1**, 6942.
32. Y. C. Cheng, K. H. Wu, F. H. Liu, J. J. Guo, X. H. Liu, G.J. Xu and P. Cai, *ACS Appl. Mater. Interfaces*, 2010, **2**, 621.
33. Y. Masuda, T. Yamada and K. Koumoto, *Cryst. Growth Des.*, 2008, **8**, 169.
34. L. Xu, X. Yang, Z. Zhai and W. Hou, *CrystEngComm*, 2011, **13**, 7267.
35. R. E. Bolz and G. L. Tuve, *CRC Handbook of Tables for Applied Engineering Science,* 2nd ed., CRC Press, New York, 1973.
36. Z. Xu, X. Kang, C. Li, Z. Hou, C. Zhang, D. Yang, G. Li and J. Lin, *Inorg. Chem*., 2010, **49**, 6706.
37. T. Sugimoto, *Adv. Colloid Interface Sci.*, 1987, **28**, 65.
38. J. W. Mullin, *Crystallization*, 4th ed., Butterworth-Heinemaan, Oxford, 2001.
39. J. Guan, L. Liu, Z. Sun and Y. Zhang, *CrystEngComm*, 2011, **13**, 2636.
40. X. Wang, M. Chen, Y. He and J. Zhu, *J. Alloy. Compd.,* 2015, **628**, 50.
41. S. Fang, Y. Xin, L. Ge, C. Han, P. Qiu and L. Wu, *Appl. Catal. B: Environ*, 2015, **179**, 458.
42. N. Wetchakun, S. Chaiwichain, B. Inceesungvorn, K. Pingmuang, S. Phanichphant, A. I. Minett and J. Chen, *ACS Appl. Mater. Interfaces*, 2012, **4**, 3718.
43. K. S. W. Sing, *Pure & Appl. Chem*., 1982, **54**, 2201.
44. J. G. Yu, Y. R. Su and B. Cheng, *Adv. Funct. Mater.*, 2007, **17**, 1984.